

Supplementary information

Regulating the Electrochemical Reduction Kinetics by Steric Hindrance Effect for Robust Zn Metal Anode

Shuo Yang^{1, a}, Ao Chen^{1, a}, Zijie Tang^{4, a}, Zhuoxi Wu¹, Pei Li¹, Yanbo Wang¹, Xiaoqi Wang^{5 *}, Xu Jin⁵, Shengchi Bai⁵, Chunyi Zhi^{1, 2, 3, 4 *}

¹ Department of Materials Science and Engineering, City University of Hong Kong, 83 Tat Chee Avenue, Hong Kong, China

² Hong Kong Institute for Advanced Study, City University of Hong Kong, Kowloon, Hong Kong, 999077, China

³ Center for Advanced Nuclear Safety and Sustainable Development, City University of Hong Kong, Kowloon, Hong Kong, 999077, China

⁴ Songshan Lake Materials Laboratory, Dongguan, Guangdong, 523808 China

⁵ Research Institute of Petroleum Exploration & Development (RIPED), PetroChina, No. 20 Xueyuan Road Haidian District, Beijing, 100083, P. R. China

* Email address: wangxq07@petrochina.com.cn; cy.zhi@cityu.edu.hk

^a These authors contributed equally to this work

Methods

Electrolyte preparation. All the salts and solvents in the electrolytes were used without further purification. The electrolyte was prepared by dissolving the desired salts ($\text{Zn}(\text{TFSI})_2$, 1M) into different solvents. For the EMC+ H_2O electrolyte, the volume ratio between water and EMC solvents is 1:1. For the TBP electrolyte, the volume ratio between water, EMC, and TBP solvents is 1:0.5:0.5.

Cathode preparation. Mn^{2+} expanded hydrated V_2O_5 (MnVO) cathode material with a micro-flower-like shape was prepared according to a previous study.¹ Specifically, 2 mmol of V_2O_5 was dissolved in a mixture of 50 mL H_2O and 2 mL H_2O_2 , and 1 mmol of $\text{MnSO}_4 \cdot 4\text{H}_2\text{O}$ was dissolved separately into 30 mL H_2O . The two solutions were admixed and transferred to a 100 Teflon lined stainless steel autoclave and heated to and held at 120 °C for 6 h. Brick red precipitates were collected by centrifugation and washed with water and ethanol three times. The collected precipitates were dried at 70 °C overnight. To prepare the cathode, a slurry composed of active material, Ketjenblack, and poly(1,1-difluoroethylene) (PVDF) with a weight ratio of 70:20:10 was coated onto a Ti mesh, which was then dried at 60 °C for 12 hours. For the cathode with high mass loading, the prepared cathode was pressed by a rolling machine before use.

Electrochemical Characterizations. Half-cells and full cells were assembled using bare Zn as the anode in CR-2032 coin cells, and glass fiber (Waterman-1820) was utilized as the separator. Before testing, the Zn foil was polished to remove the surface oxide layer and cut into different sizes (1 cm*1 cm for the coin cell and 6 cm*6 cm for

the pouch cell).

For the pouch cell, MnVO coating on a Ti mesh (6 cm * 6 cm) with a mass loading of 390 mg was used as a cathode. Zn foil with a thickness of 100 μm was used as the anode, while a glass fiber (Waterman-1820) was employed as the separator. The sealing process was carried out using an automated vacuum sealing machine (Wuhan Geruisi New Energy Co., Ltd) with two layers of Al soft packaging films. All assembly procedures were conducted under ambient conditions at room temperature ($\sim 25\text{ }^{\circ}\text{C}$). The batteries were positioned between the testing plates with a pressure of 0.1 MPa applied to ensure uniform external pressure.

The galvanostatic charging-discharging processes based on different current densities were conducted using the Land battery testing system (Wuhan, China) and the Neware battery testing system (Neware, Shenzhen, China). The cyclic voltammogram (CV), Tafel plot, electrochemical impedance spectroscopy (EIS), and linear sweep voltammetry (LSV) were measured using a CHI-760 electrochemical working station. For the Tafel plot, a rotating disk electrode was used as the working electrode, an Ag/AgCl electrode was used as the reference electrode, and a Pt foil was used as the counter electrode. The test was measured under a rotating speed of 3600 rpm to eliminate the effect of mass transfer. EIS measurement was conducted with a 5 mV amplitude AC signal with frequency ranging from 100 kHz to 0.01 Hz.

Characterizations. The crystal structure and phase composition were characterized by X-ray diffraction (XRD) using Rigaku X-ray Diffractometer SmartLabTM 9kW (Cu $K\alpha$, $\lambda = 0.154\text{ nm}$). The micromorphology of products was investigated by scanning

electron microscope (SEM, ESEM, FEI/Philips XL30) and transmission electron microscopy (TEM) using an FEI Tecnai G2 f20 s-twin at 200kV. The X-ray Photoelectron Spectrometer (XPS) studies were performed using a PHI5000 VersaProbe II photoelectron spectrometer, and the spectra were calibrated using a carbon spectrum as a reference. Raman spectra measurements were operated using the WITec alpha300 Raman System. Fourier Transform infrared spectroscopy measurements were conducted using a PerkinElmer FTIR Spectrometer. The ^1H NMR spectra were acquired on a Bruker AVANCE III HD 400 NMR spectrometer using deuterated DMSO as the field frequency lock. The viscosities of different electrolytes were measured by using the falling-ball viscometer (Anton Paar, Lovis 2000 M/ME).

Computational details: The electrostatic potential (ESP) calculation was conducted using the DMol3 package. The structure optimization and calculations were described using the B3LYP hybrid functional, and the Grimme method was used for dispersion-corrected density functional theory calculations (DFT-D). DFT semicore pseudopotentials core treatment was implemented for relativistic effects, replacing core electrons with a single effective potential. Double numerical plus polarization was employed as the basis set. The convergence tolerance of energy of 10^{-6} Hartree was taken (1 Hartree = 27.21 eV), and the maximal allowed force and displacement were 0.002 and 0.005 Hartree \AA^{-1} , respectively.

MD simulations were performed by the Forcite module in Materials Studio to explore the solvation structure of Zn^{2+} in different electrolytes. The used forcefield was COMPASSII for all subsequent simulations. All the simulations were performed with

constant temperature (298.15 K) in a cubic box with periodic boundary conditions in all three Cartesian directions. NPT ensembles initially equilibrated bulk electrolytes for 4 ns. In this stage, the Velocity-Rescale thermostat and the Berendsen barostat were used to control the system temperature and pressure. Electrostatic interactions were treated using the Ewald sums, and Van der Waals (vdW) interactions were adopted using cut-off methods with a cut-off radius of 12.5 Å. After that, a 6 ns production run in an NVT ensemble under a Nose-Hoover thermostat was finally conducted. Electrostatic interactions were treated using the Ewald sums, and Van der Waals (vdW) interactions were adopted using cut-off methods with a cut-off radius of 18.5 Å. Only the final 1 ns was sampled for radial distribution function (RDF) and coordination structure counting analyses.

Supplementary Notes

The electron transfer reorganization energies (λ) can be expressed as a dielectric continuum formulation:

$$\lambda = q^2 \left(\frac{1}{a} - \frac{1}{R} \right) \left(\frac{1}{\epsilon_{op}} - \frac{1}{\epsilon_{st}} \right)$$

The reorganization energies in pristine aqueous, EMC+H₂O, and TBP electrolytes are λ_a , λ_e , and λ_t , respectively. For Zn²⁺ ion, a is 0.74 Å. R is the distance of solvated Zn²⁺ to the electrode surface. Here, as IHP only constitutes a molecular layer, R is approximately the radius of the solvated Zn²⁺. So, for pristine aqueous, EMC+H₂O, and TBP electrolytes, the R is 2.5 Å, 4 Å and 7 Å, respectively. The electrostatic constant of a mixed solution can be calculated using the following formula:^{2,3}

$$\epsilon_m = \phi_a \epsilon_a + \phi_b \epsilon_b + \phi_c \epsilon_c$$

The ϵ_m , ϵ_a , ϵ_b and ϵ_c are the dielectric constants of the mixture and solvents a, b and c, respectively. ϕ_a , ϕ_b and ϕ_c are the volume fractions of solvents a, b and c in the mixture.

As a result, the calculated $\lambda_t=1.16\lambda_a$ and $\lambda_e=1.06\lambda_a$.

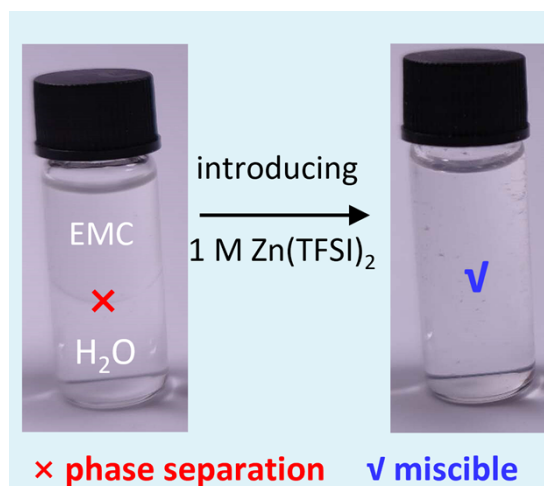


Figure S1. Digital photos of EMC mixture before (left) and after (right) introducing EMC solvent. The TFSI⁻ anion consists of the hydrophobic -CF₃ and the hydrophilic -S=O groups, allowing it to function as a surfactant to facilitate interactions with H₂O and EMC. As a result, it promotes the miscibility between the hydrophobic EMC and H₂O.

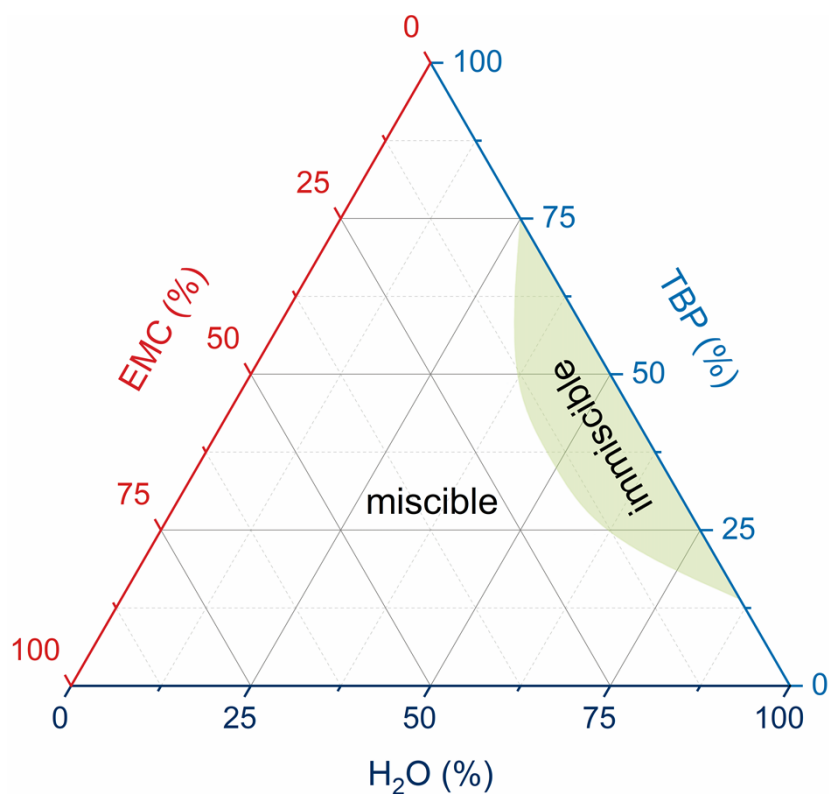


Figure S2. The miscibility of different solvents with varying volume ratios after adding 1 M Zn(TFSI)₂.

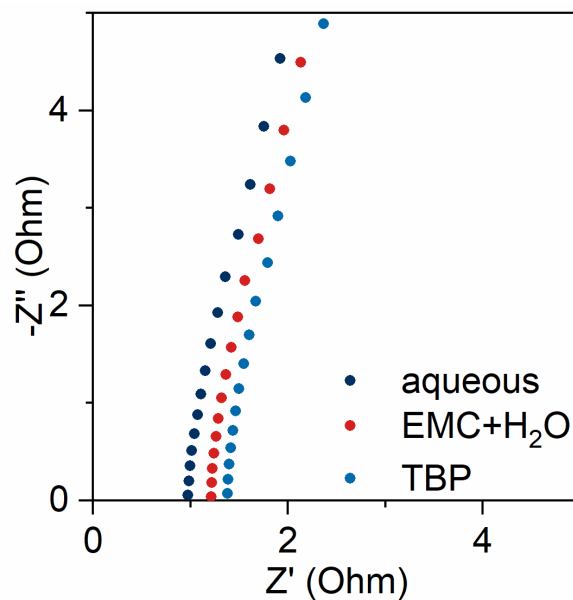


Figure S3. AC impedance spectra of the stainless steel||SS batteries with different electrolytes. The ionic conductivity of aqueous, EMC+H₂O, and TBP electrolytes was measured according to the following equation:

$$\sigma = \frac{l}{RA}$$

Where l is the interval distance between the two SS electrodes, R is the bulk resistance, and A is the contact area of the electrolyte. The calculated ionic conductivities for aqueous, EMC, and TBP electrolytes are 35.4, 29.4, and 25.0 mS cm⁻¹, respectively (Table S1).

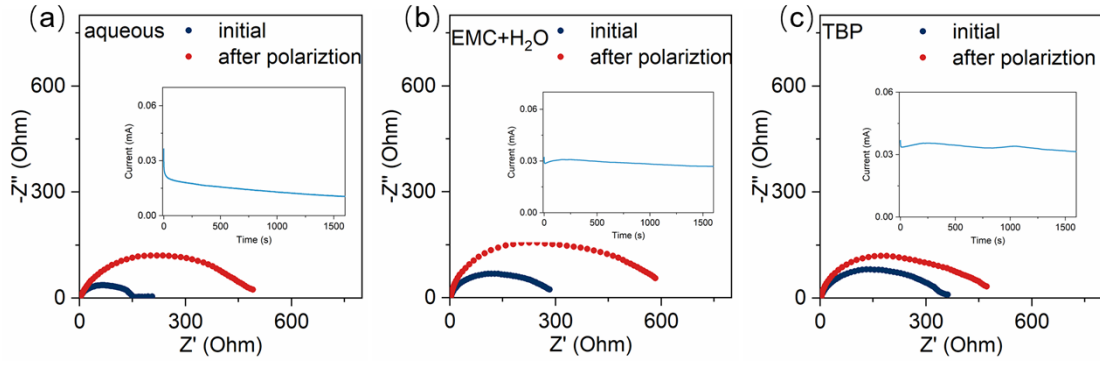


Figure S4. AC impedance spectra of symmetric Zn cells with (a) aqueous, (b) EMC+H₂O, and (c) TBP electrolytes before and after a constant potential of 5 mV for 1600 s. The insets are the current-time corresponding plots.

The following equation calculates the cation transport number (t):

$$t = \frac{I_s(\Delta V - I_0 R_0)}{I_0(\Delta V - I_s R_s)}$$

where ΔV is the constant polarization voltage applied (5 mV), I_0 and R_0 are the initial current and resistance, I_s and R_s are the steady-state current and resistance, respectively.

The calculated cation transport numbers for aqueous, EMC, and TBP electrolytes are 0.23, 0.31, and 0.47, respectively (Table S1).

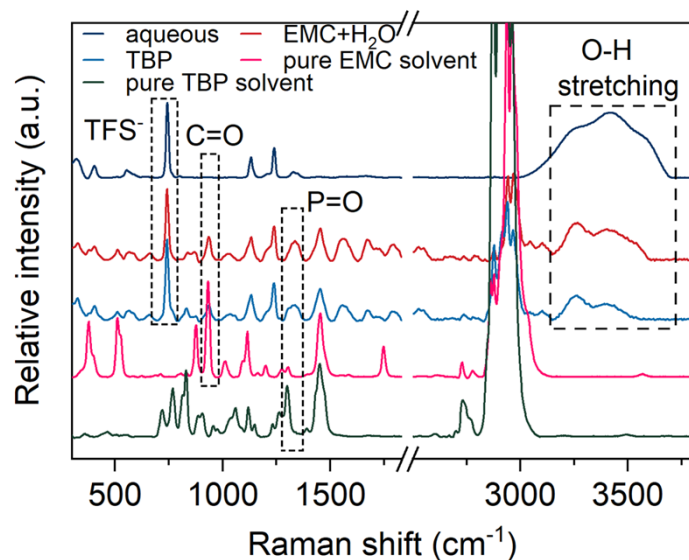


Figure S5. Raman spectra of different electrolytes and solvents. The C=O and P=O characteristic peak in the TBP electrolyte indicates the successful introduction of EMC and TBP into the solvation structure. The decreased peaks attributed to the O-H stretching ($3000\text{--}3700\text{ cm}^{-1}$) in the TBP electrolyte demonstrate the interruption of hydrogen bonding owing to the interaction between water and EMC and TBP solvents.

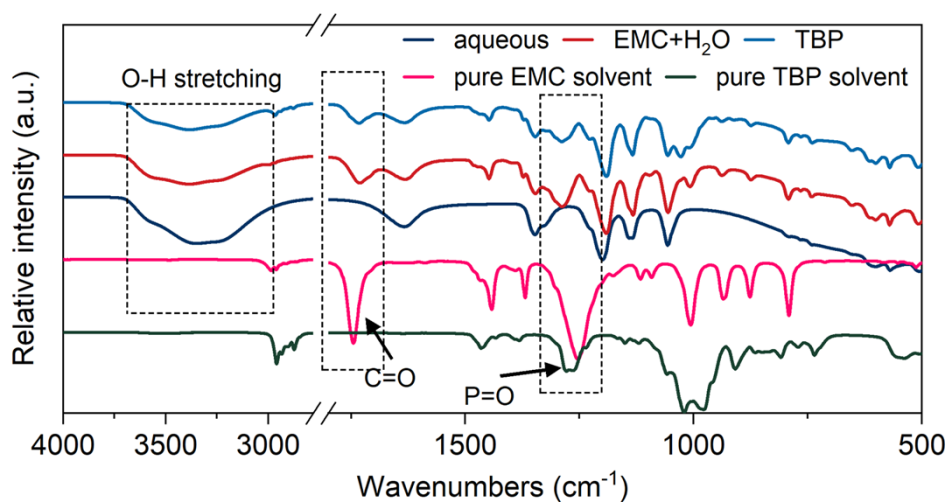


Figure S6. FTIR spectra of different electrolytes and solvents.

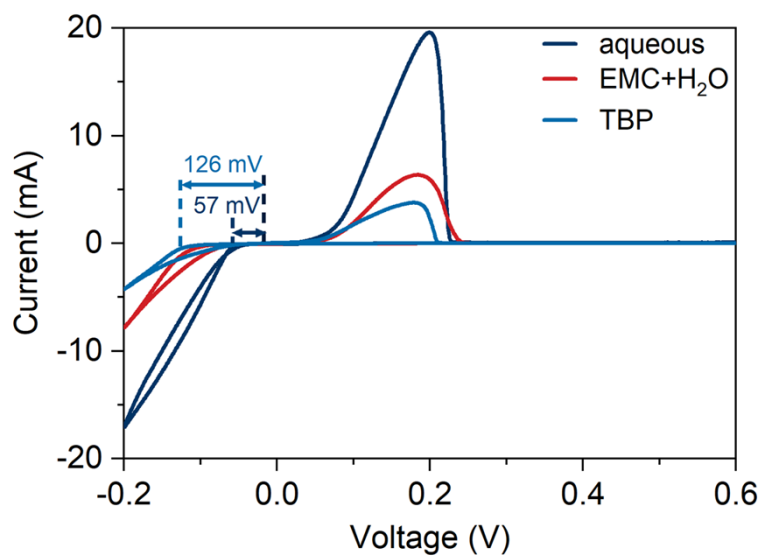


Figure S7. Cyclic voltammograms of the Zn||Cu half-cells in different electrolytes at a scan rate of 2 mV s⁻¹.

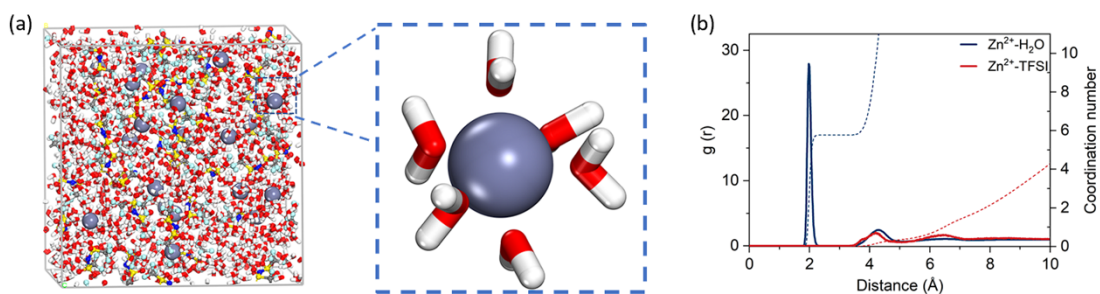


Figure S8. (a) Snapshot of the pristine aqueous electrolyte obtained from MD simulations and partially enlarged snapshot representing the Zn²⁺ solvation structure. (b) RDFs and coordination collected from MD simulations in the pristine aqueous electrolyte.

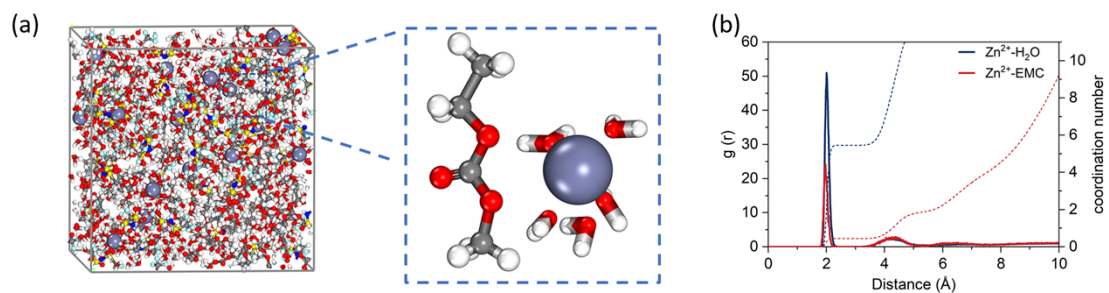


Figure S9. (a) Snapshot of EMC+H₂O electrolyte obtained from MD simulations and partially enlarged snapshot representing the Zn²⁺ solvation structure. (b) RDFs and coordination collected from MD simulations in EMC+H₂O electrolyte.

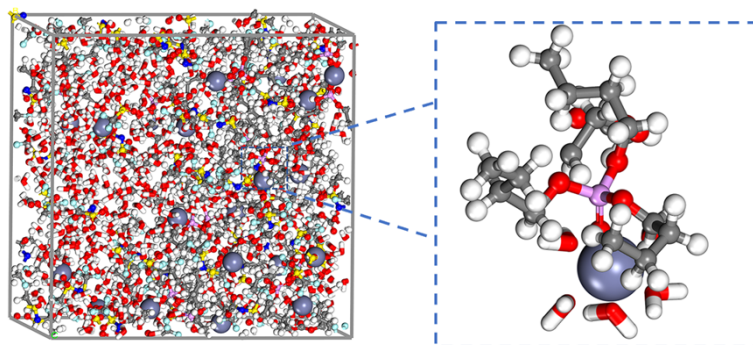


Figure S10. Snapshot of TBP electrolyte obtained from MD simulations and partially enlarged snapshot representing the Zn²⁺ solvation structure.

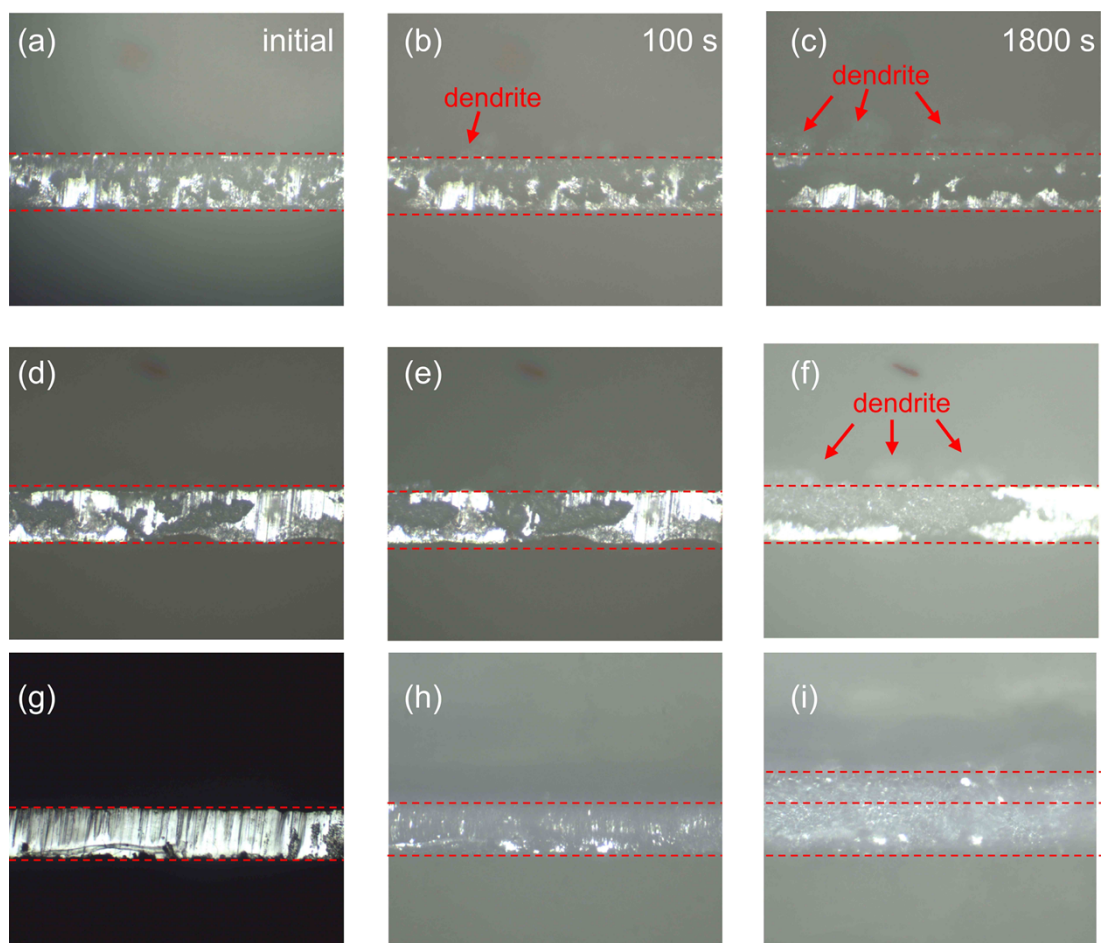


Figure S11. In-situ optical images of Zn deposition with (a), (b), and (c) aqueous, (d), (e), and (f) EMC+H₂O, (g), (h) and (i) TBP electrolytes at a current density of 10 mA cm⁻².

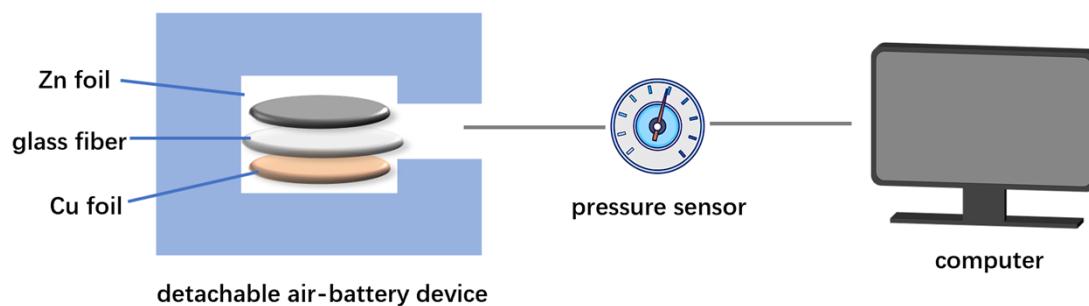


Figure S12. Schematic illustration of *operando* gas pressure measurement.

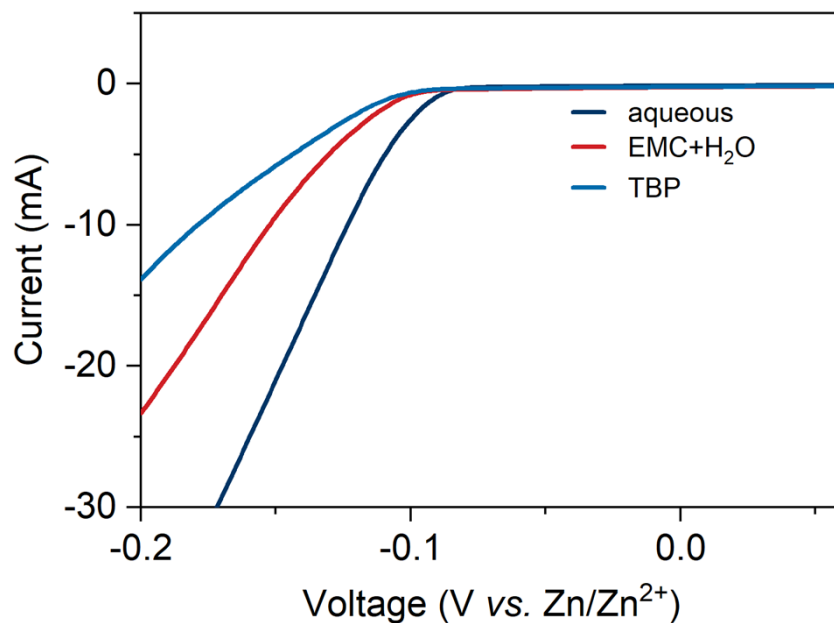


Figure S13. LSV curves of Zn||stainless steel batteries with different electrolytes at a scan rate of 5 mV s^{-1} .

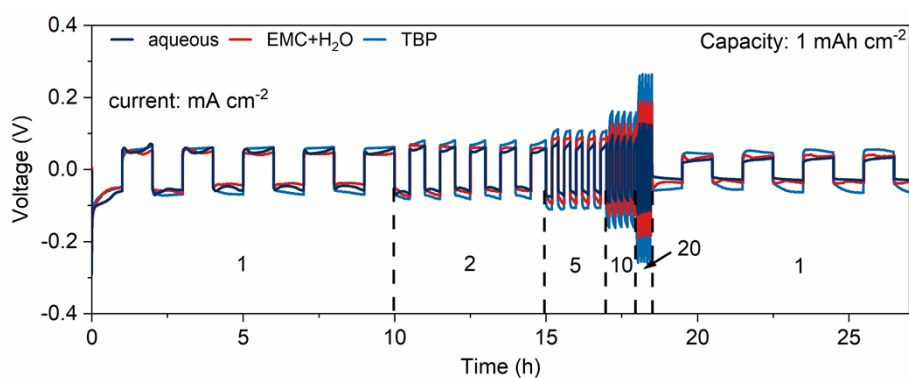


Figure S14. The voltage profiles of Zn||Zn cells in different electrolytes operated at current densities ranging from 1 mA cm^{-2} to 20 mA cm^{-2} .

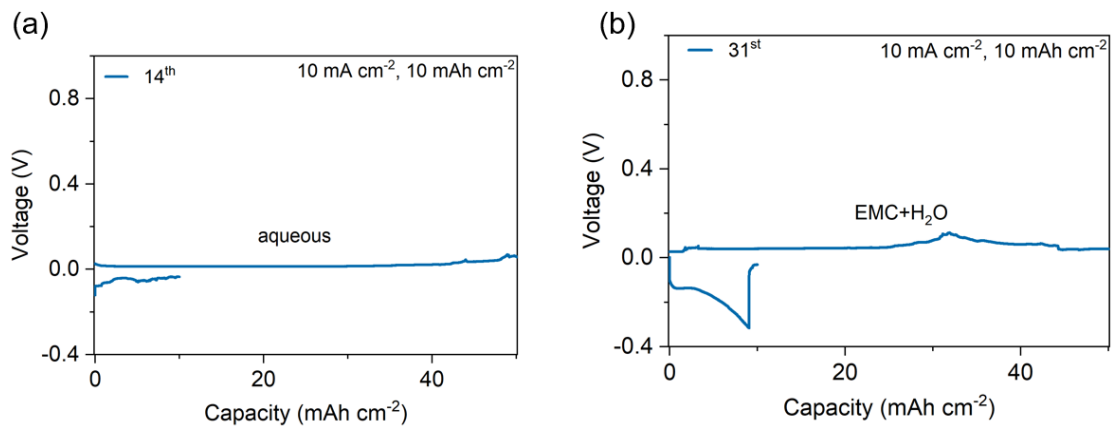


Figure S15. Voltage profiles of Zn||Cu cells cycled in (a) pristine aqueous and (b) EMC+H₂O electrolytes after battery failures.

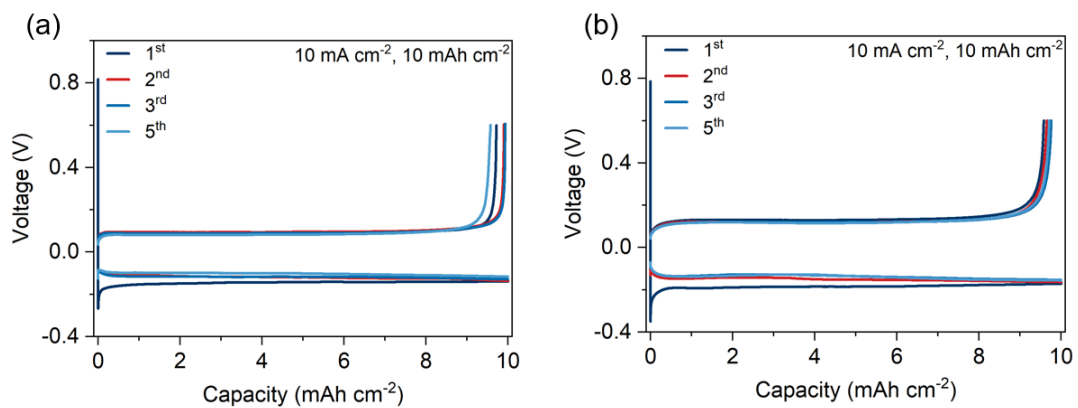


Figure S16. Voltage profiles of Zn||Cu cells of the first 5th cycles in the (a) aqueous and (b) EMC+H₂O electrolytes.

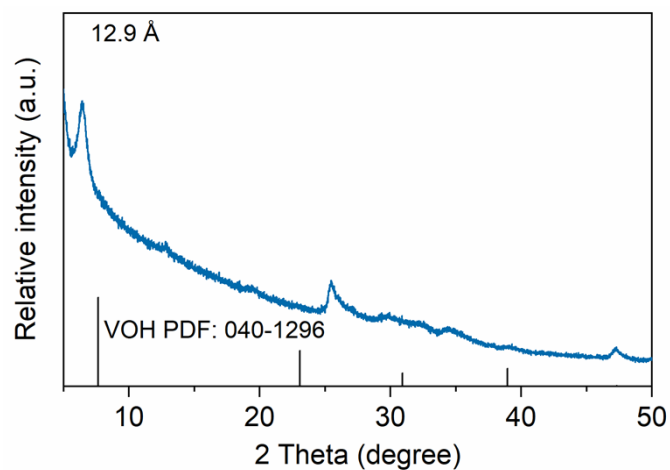


Figure S17. XRD pattern of the as-prepared Mn^{2+} expanded hydrated V_2O_5 . The Miller indices corresponding to the crystallographic planes do not exist in the current database. However, the diffraction peaks are consistent with the previous report.¹

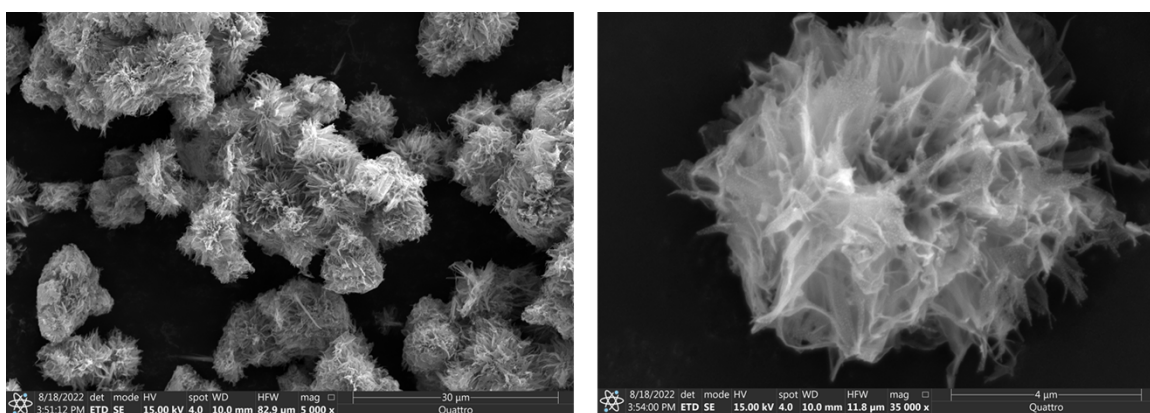


Figure S18. SEM images of the as-prepared Mn^{2+} expanded hydrated V_2O_5 .

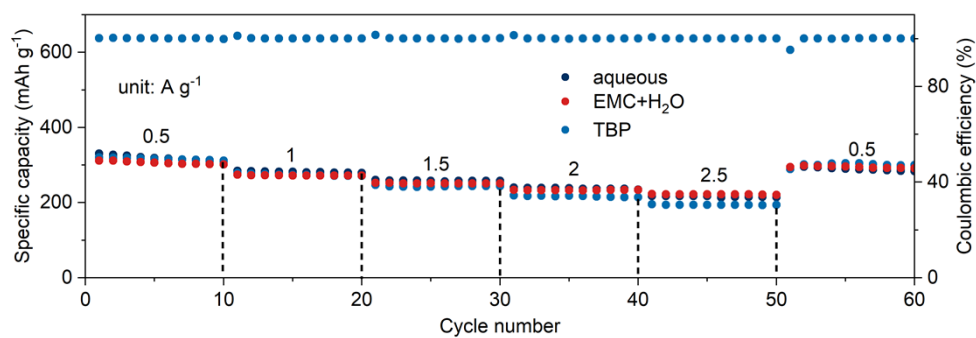


Figure S19. Rate performance of Zn||MnVO batteries with different electrolytes.

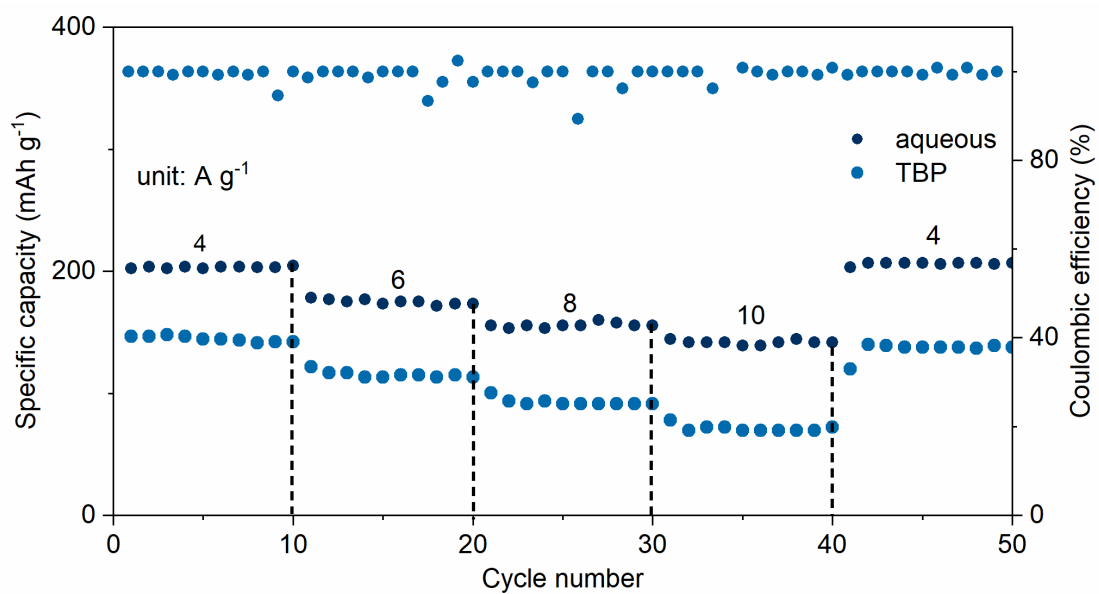


Figure S20. Rate performance of Zn||MnVO batteries with different electrolytes at current densities of 4, 6, 8, and 10 A g⁻¹.

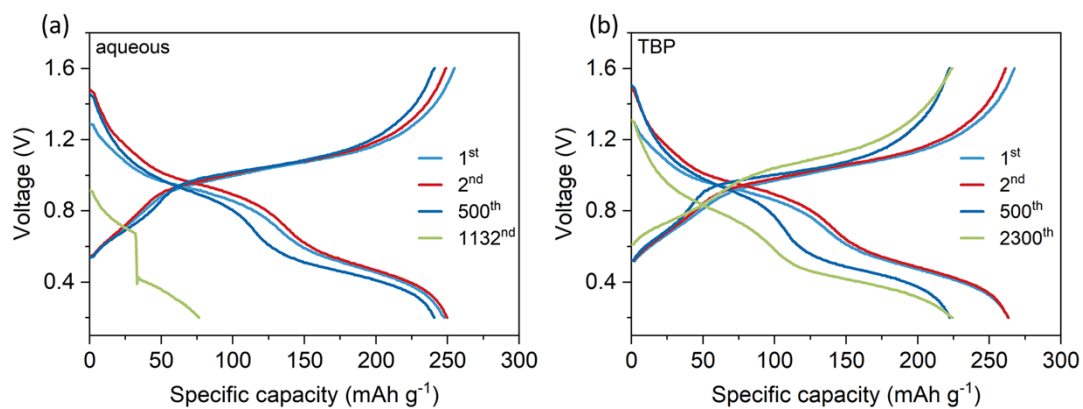


Figure S21. GCD curves of the Zn||MnVO full cell based on the (a) pristine aqueous and (b) TBP electrolytes.

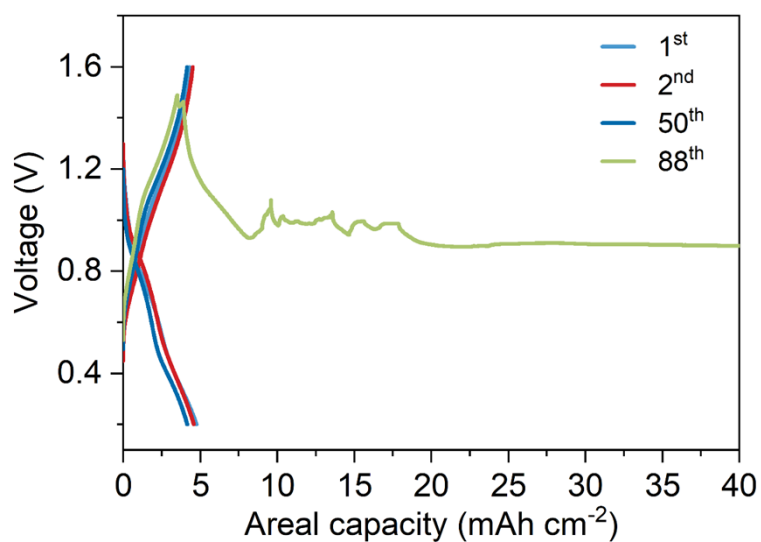


Figure S22. GCD curves of the Zn||MnVO full cell based on the pristine aqueous electrolyte with a high mass loading.

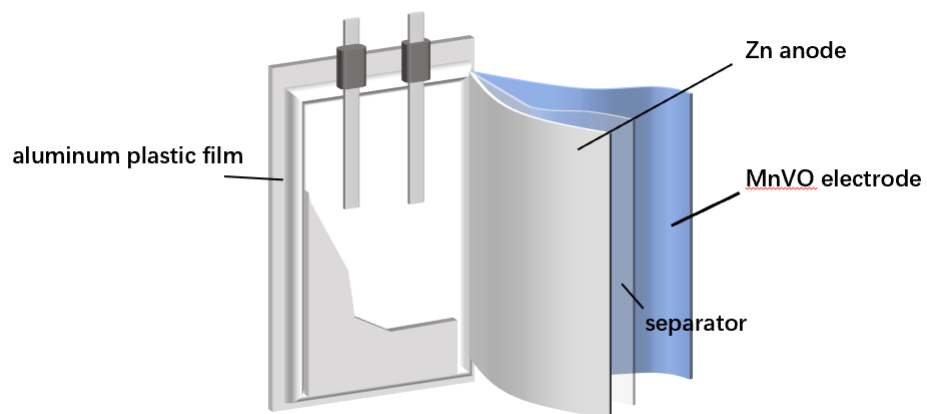


Figure S23. The schematic illustration of the assembled pouch cell.

Table S1 Summary of different electrolytes

Electrolyte	Viscosity (mPa s)	Ionic conductivity (mS cm⁻¹)	Zn²⁺ transport numbers
aqueous	2.14	39.4	0.23
EMC+H ₂ O	3.36	29.4	0.31
TBP	5.77	25.0	0.44

Table S2 Performance comparison of reported unsymmetric half-cells

Additive	Current density (mA cm ⁻²)	Areal capacity (mAh cm ⁻²)	Cumulative capacity (mAh cm ⁻²)	Reference
propylene carbonate (PC)	1	0.5	500	4
hexaoxacyclooctadecane (18C6)	1	0.5	200	5
N, N-dimethylformamidium trifluoromethanesulfonate (DOTf)	4	4	2000	6
Methanol (MeOH)	2.93	2.93	820	7
propylene glycol (PG)	4	2	2640	8
molecular sieve (ZSM-5)	1	1	2000	9
cerium chloride (CeCl ₃)	10	10	1200	10
lanthanum nitrate (La ³⁺ -ZS)	2	1	4200	11
phytic acid	2	1	1600	12
2-Bis(2-hydroxyethyl) amino-2-(hydroxymethyl)-1,3-propanediol (BIS-TRIS)	1	1	800	13
potassium hexafluorophosphate (KPF ₆)	4	2	400	14
sodium anthraquinone-2-sulfonate (AQS)	2	1	1200	15
sulfolane	2	1	1250	16
poly(acrylamide-co-methyl acrylate)	1	1	300	17
C ₃ N ₄ quantum dots	0.5	0.5	200	18
formamide	0.5	0.5	550	19
TBP with steric hindrance effect	10	10	3000	This work

Table S3 Performance comparison of areal capacity with other reported Zn-ion batteries

Cathode	Mass loading	Maximum Areal capacity (mAh cm ⁻²)	Cycle numbers	Reference
Mg _{0.26} V ₂ O ₅ ·0.73H ₂ O	5	2.12	100	20
Na ₂ V ₆ O ₁₆ ·3H ₂ O	12.5	3.1	416	21
V ₂ O ₅	5.4	1.1	400	22
VOH	22.9	5.2	100	23
I ₂	-	5	275	24
MnO ₂ @N-C@CC	6	1.1	150	25
MnO ₂	19	2.93	100	26
MoS ₂	11.5	0.87	50	27
K _{0.27} MnO ₂ ·0.54H ₂ O	8	0.795	400	28
3,4,9,10- perylene-tetracarboxylic dianhydride	12.3	1.26	500	29
MnVO	16	5.4	650	This work

Reference

1. C. Liu, Z. Neale, J. Zheng, X. Jia, J. Huang, M. Yan, M. Tian, M. Wang, J. Yang and G. Cao, *Energy Environ. Sci.*, 2019, **12**, 2273-2285.
2. T. NAGAI and S. PRAKONGPAN, *Chem. Pharm. Bull.*, 1984, **32**, 340-343.
3. A. Jouyban, S. Soltanpour and H.-K. Chan, *Int. J. Pharm.*, 2004, **269**, 353-360.
4. F. Ming, Y. Zhu, G. Huang, A.-H. Emwas, H. Liang, Y. Cui and H. N. Alshareef, *J. Am. Chem. Soc.*, 2022, **144**, 7160-7170.
5. R. Li, M. Li, Y. Chao, J. Guo, G. Xu, B. Li, Z. Liu, C. Yang and YanYu, *Energy Storage Mater.*, 2022, **46**, 605-612.
6. C. Li, A. Shyamsunder, A. G. Hoane, D. M. Long, C. Y. Kwok, P. G. Kotula, K. R. Zavadil, A. A. Gewirth and L. F. Nazar, *Joule*, 2022, **6**, 1103-1120.
7. L. Ma, J. Vatamanu, N. T. Hahn, T. P. Pollard, O. Borodin, V. Petkov, M. A. Schroeder, Y. Ren, M. S. Ding, C. Luo, J. L. Allen, C. Wang and K. Xu, *Proceedings of the National Academy of Sciences*, 2022, **119**, e2121138119.
8. Y. Shang, P. Kumar, T. Musso, U. Mittal, Q. Du, X. Liang and D. Kundu, *Adv. Funct. Mater.*, 2022, DOI: 10.1002/adfm.202200606.
9. J. Zhu, Z. Bie, X. Cai, Z. Jiao, Z. Wang, J. Tao, W. Song and H. J. Fan, *Adv. Mater.*, 2022, **34**, 2207209.
10. Z. Hu, F. Zhang, Y. Zhao, H. Wang, Y. Huang, F. Wu, R. Chen and L. Li, *Adv. Mater.*, 2022, **34**, 2203104.
11. R. Zhao, H. Wang, H. Du, Y. Yang, Z. Gao, L. Qie and Y. Huang, *Nat. Commun.*, 2022, **13**, 3252.

12. H. Liu, J.-G. Wang, W. Hua, L. Ren, H. Sun, Z. Hou, Y. Huyan, Y. Cao, C. Wei and F. Kang, *Energy Environ. Sci.*, 2022, **15**, 1872-1881.
13. M. Luo, C. Wang, H. Lu, Y. Lu, B. B. Xu, W. Sun, H. Pan, M. Yan and Y. Jiang, *Energy Storage Mater.*, 2021, **41**, 515-521.
14. Y. Chu, S. Zhang, S. Wu, Z. Hu, G. Cui and J. Luo, *Energy Environ. Sci.*, 2021, **14**, 3609-3620.
15. R. Sun, D. Han, C. Cui, Z. Han, X. Guo, B. Zhang, Y. Guo, Y. Liu, Z. Weng and Q.-H. Yang, *Angew. Chem. Int. Ed.*, e202303557.
16. C. Huang, X. Zhao, Y. Hao, Y. Yang, Y. Qian, G. Chang, Y. Zhang, Q. Tang, A. Hu and X. Chen, *Energy Environ. Sci.*, 2023, **16**, 1721-1731.
17. B. Niu, Z. Li, D. Luo, X. Ma, Q. Yang, Y.-E. Liu, X. Yu, X. He, Y. Qiao and X. Wang, *Energy Environ. Sci.*, 2023, **16**, 1662-1675.
18. W. Zhang, M. Dong, K. Jiang, D. Yang, X. Tan, S. Zhai, R. Feng, N. Chen, G. King, H. Zhang, H. Zeng, H. Li, M. Antonietti and Z. Li, *Nat Commun*, 2022, **13**, 5348.
19. C. You, R. Wu, X. Yuan, J. Ye, L. Liu, L. Fu, P. Han and Y. Wu, *Energy Environ. Sci.*, 2023, DOI: 10.1039/D3EE01741A.
20. N. Wang, C. Sun, X. Liao, Y. Yuan, H. Cheng, Q. Sun, B. Wang, X. Pan, K. Zhao, Q. Xu, X. Lu and J. Lu, *Adv. Energy Mater.*, 2020, **10**, 2002293.
21. H. Wang, H. Li, Y. Tang, Z. Xu, K. Wang, Q. Li, B. He, Y. Liu, M. Ge, S. Chen, T. Hao, G. Xing and Y. Zhang, *Adv. Funct. Mater.*, 2022, **32**, 2207898.
22. C. Huang, F. Huang, X. Zhao, Y. Hao, Y. Yang, Y. Qian, G. Chang, Y. Zhang,

- Q. Tang, A. Hu and X. Chen, *Adv. Funct. Mater.*, 2023, **33**, 2210197.
23. G. Ma, S. Di, Y. Wang, W. Yuan, X. Ji, K. Qiu, M. Liu, X. Nie and N. Zhang, *Energy Storage Mater.*, 2023, **54**, 276-283.
24. M. Yan, N. Dong, X. Zhao, Y. Sun and H. Pan, *ACS Energy Lett.*, 2021, **6**, 3236-3243.
25. Y. Gao, Q. Cao, J. Pu, X. Zhao, G. Fu, J. Chen, Y. Wang and C. Guan, *Adv. Mater.*, 2023, **35**, 2207573.
26. J. Dong, H. Peng, J. Wang, C. Wang, D. Wang, N. Wang, W. Fan, X. Jiang, J. Yang and Y. Qian, *Energy Storage Mater.*, 2023, **54**, 875-884.
27. Z. Yao, W. Zhang, X. Ren, Y. Yin, Y. Zhao, Z. Ren, Y. Sun, Q. Lei, J. Wang, L. Wang, T. Ji, P. Huai, W. Wen, X. Li, D. Zhu and R. Tai, *ACS Nano*, 2022, **16**, 12095-12106.
28. R. Guo, X. Liu, F. Xia, Y. Jiang, H. Zhang, M. Huang, C. Niu, J. Wu, Y. Zhao, X. Wang, C. Han and L. Mai, *Adv. Mater.*, 2022, **34**, 2202188.
29. H. Zhang, Y. Fang, F. Yang, X. Liu and X. Lu, *Energy Environ. Sci.*, 2020, **13**, 2515-2523.